under Air Force contract no. FA8721-05-C-0002; by the U.S. Army Research Office grant no. W911NF-14-1-0682; and by NSF grant no. PHY-1415514. The views and conclusions contained herein are those of the authors and should not be interpreted as necessarily representing the official policies or endorsements, either expressed or implied, of ODNI, IARPA, or the U.S. government. G.C. acknowledges partial support by the European Union (EU) under Research Executive Agency (REA) grant agreement no. CIG-618258. J.By. acknowledges partial support by the EU under REA grant agreement no. CIG-618353.

SUPPLEMENTARY MATERIALS

www.sciencemag.org/content/354/6319/1573/suppl/DC1
Supplementary Text
Figs. S1 to S4
References (*32*–*37*)

18 July 2016; accepted 21 November 2016
Published online 8 December 2016
10.1126/science.aah5844

QUANTUM OPTICS

Quantum optical circulator controlled by a single chirally coupled atom

Michael Scheucher, Adèle Hilico, Elisa Will, Jürgen Volz,* Arno Rauschenbeutel*

Integrated nonreciprocal optical components, which have an inherent asymmetry between their forward and backward propagation direction, are key for routing signals in photonic circuits. Here, we demonstrate a fiber-integrated quantum optical circulator operated by a single atom. Its nonreciprocal behavior arises from the chiral interaction between the atom and the transversally confined light. We demonstrate that the internal quantum state of the atom controls the operation direction of the circulator and that it features a strongly nonlinear response at the single-photon level. This enables, for example, photon number–dependent routing and novel quantum simulation protocols. Furthermore, such a circulator can in principle be prepared in a coherent superposition of its operational states and may become a key element for quantum information processing in scalable integrated optical circuits.

As their electronic counterparts, integrated optical circuits require nonreciprocal elements, such as diodes and circulators, for signal routing and processing. Bulk optical implementations of such components are readily available and rely mostly on a nonreciprocal polarization rotation via the Faraday effect. However, this mechanism cannot straightforwardly be translated to integrated optics because nanooptical structures are typically birefringent (*1*). Demonstrations of integrated nonreciprocal devices therefore rather used, for example, nonlinear optical effects (*2*–*4*), time-modulation of the waveguide (*5*–*7*), or magneto-optical effects in conjunction with the extraordinary polarization properties of strongly confined light fields (*1*, *8*, *9*). None of these approaches could simultaneously realize strong nonreciprocity, low loss, and compatibility with low light levels. However, these characteristics are crucial when it comes to quantum applications such as quantum communication (*10*), quantum information processing (*11*), and quantum simulation (*12*). There, information is encoded in individual photons, and their loss must be avoided as much as possible. This condition narrows down the scope of quantum-compatible nonreciprocal optical elements to nonreciprocal phase shifters and circulators.

We experimentally realized a fiber-integrated circulator that is capable of routing individual photons for quantum optical applications. It is operated by a single atom that is coupled to the evanescent field of a whispering-gallery-mode (WGM) microresonator. The latter is interfaced with two coupling fibers (*13*, *14*), realizing a four-port device (Fig. 1A). We demonstrate that the internal quantum state of the atom controls the operation direction of the circulator. Furthermore, we show that being controlled by a single atom, our device features photon number–dependent routing capability that has application in, for example, novel quantum simulation protocols.

In order to achieve efficient routing, the coupling rates κ_a and κ_b between the resonator field and the field in the respective coupling fiber "a" or "b" are adjusted so that both fibers are approximately critically coupled to the empty resonator: $\kappa_a \approx \kappa_b \gg \kappa_0$, where κ_0 is the intrinsic resonator field decay rate. When no atom is coupled to the resonator mode, this realizes an add-drop filter (*13*, *14*) in which light that is launched into one fiber will be transferred to the other fiber via the resonator. Because of its strong transverse confinement, the evanescent field of the clockwise (cw) propagating resonator mode is almost fully circularly polarized (*15*). Its electric field vector rotates counterclockwise in the plane orthogonal to the resonator axis (z axis), corresponding to σ^- polarization (Fig. 1B). Time-reversal symmetry then implies that the evanescent field of the counterclockwise (ccw) propagating mode is almost fully σ^+-polarized (*15*). Coupling such "spin orbit–locked" light fields to single quantum emitters gives rise to the new paradigm of chiral quantum optics (*16*). In the context of WGMs, it recently enabled the implementation of an optical switch controlled by a single photon (*17*) and the extraction of a single photon from an optical pulse (*18*). Moreover, an optical isolator was realized that either transmits or dissipates fiber-guided light depending on its propagation direction (*19*). For the circulator, we resonantly coupled a single ^{85}Rb atom to the resonator, which is prepared in the outermost Zeeman sublevel $m_F = +3$ of the $5S_{1/2}$, $F = 3$ hyperfine ground state. Thus, the two counter-propagating resonator modes couple to an effective V-level system (Fig. 1C). Remarkably, the strength of the transition to the $5P_{3/2}$, $F' = 4$, $m_{F'} = +4$ excited state is 28 times stronger than that to the $F' = 4$, $m_{F'} = +2$ state (*20*). As a consequence, light in the ccw mode interacts strongly with the atom with a coupling strength g_{ccw}, whereas light in the cw mode exhibits much weaker coupling, $g_{cw} \ll g_{ccw}$. This chiral (direction-dependent) light-matter interaction breaks Lorentz reciprocity (*19*, *21*–*25*). In particular, the presence of the atom changes the resonator field decay rate from $\kappa_{tot} = \kappa_0 + \kappa_a + \kappa_b$ to $\kappa_{tot} + \Gamma_{cw/ccw}$, where $\Gamma_{cw/ccw} = g^2_{cw/ccw}/\gamma$ is the direction-dependent atom-induced loss rate (*26*) and $\gamma = 2\pi \times 3$ MHz is the dipole decay rate of Rb. For light in the cw mode, Γ_{cw} is small, and the field decay rate is not substantially modified by the atom, whereas for the ccw mode, Γ_{ccw} can become comparable with or even exceed κ_{tot}. Consequently, the add-drop functionality is maintained when light is launched into those fiber ports for which it couples to the cw mode (Fig. 1D, input ports 2 and 4). However, for the two other input ports (Fig. 1D, 1 and 3), the light couples to the ccw mode, and the resonator-atom system operates in the undercoupled regime

$$\kappa_a, \kappa_b \ll \Gamma_{ccw} \quad (1)$$

Thus, the incident light field remains in its initial fiber. Overall, the device thus realizes an optical circulator that routes light from the input port i to the adjacent output port $i + 1$ with $i \in \{1, 2, 3, 4\}$ (Fig. 1D). Preparing the atom in the opposite Zeeman ground state, $F = 3$, $m_F = -3$, exchanges the roles of the cw and ccw mode and thus yields a circulator with reversed operation direction. Hence, the circulator is programmable, and its operation direction is defined by the internal state of the atom.

For nonperfect circular polarization of the modes and our experimental parameters ($g_{ccw} \approx 2\pi \times 12$ MHz), the ratio between $\Gamma_{ccw} \approx 2\pi \times 48$ MHz and $\Gamma_{cw} \approx 2\pi \times 1.7$ MHz is finite (*26*). Concerning the performance of the circulator, there is thus a trade-off between efficient light transfer from

Vienna Center for Quantum Science and Technology, Atominstitut, Technischen Universität Wien Stadionallee 2, 1020 Vienna, Austria.
*Corresponding author. Email: jvolz@ati.ac.at (J.V.); arno.rauschenbeutel@ati.ac.at (A.R.)

one fiber to the other via the cw mode, which implies $\kappa_a, \kappa_b \gg \kappa_0 + \Gamma_{cw}$ and the condition that the presence of the atom should substantially influence the field decay rate (Eq. 1). To find the optimum working point in our experiment, we measured the circulator performance as a function of the fiber-resonator coupling strengths κ_a and κ_b, which can be adjusted by changing the distance between the respective fiber and the resonator surface. We imposed the constraint that fiber a is critically coupled to the empty resonator that is loaded with fiber b: $\kappa_a = \kappa_b + \kappa_0$ (*26*). For each setting, we measured the transmissions $T_{i,j}$ to all output ports j when sending a weak coherent probe field into the four different input ports i (*26*). The relevant transmissions as a function of κ_{tot} are shown in Fig. 2, A and B.

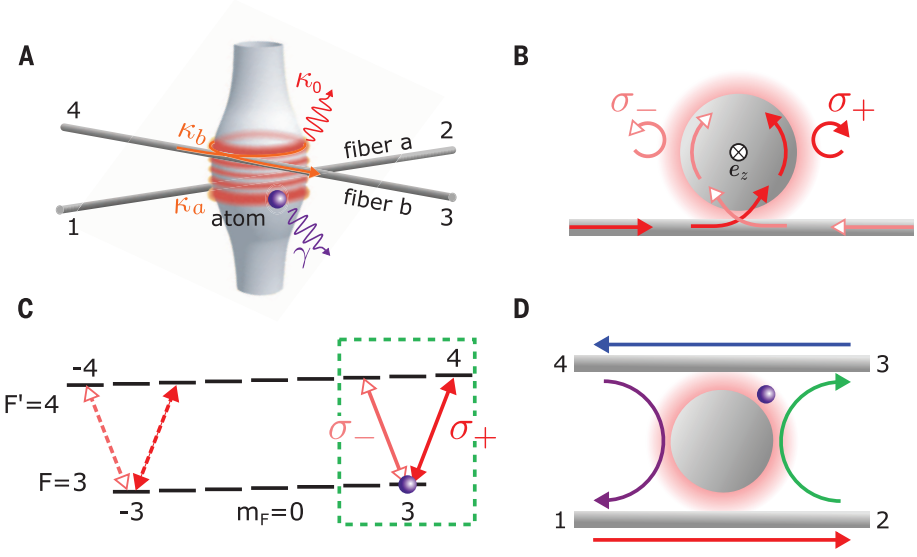

Fig. 1. Operation principle of the circulator. (**A**) Schematic of the experimental system. A single ^{85}Rb atom is coupled to the WGM of a bottle microresonator, which is interfaced by two tapered fiber couplers. (**B**) The polarization of the evanescent field of the modes, σ^- and σ^+, depends on their propagation direction, clockwise or counterclockwise. (**C**) For a ^{85}Rb atom prepared in the $F = 3$, $m_F = +3$ Zeeman state, the transition strength for σ^+-polarized light (for the counterclockwise mode) is 28 times larger than for σ^--polarized light (for the clockwise mode). This situation is reversed if the atom is prepared in $m_F = -3$. (**D**) Routing behavior of the circulator for the atom prepared in $m_F = +3$.

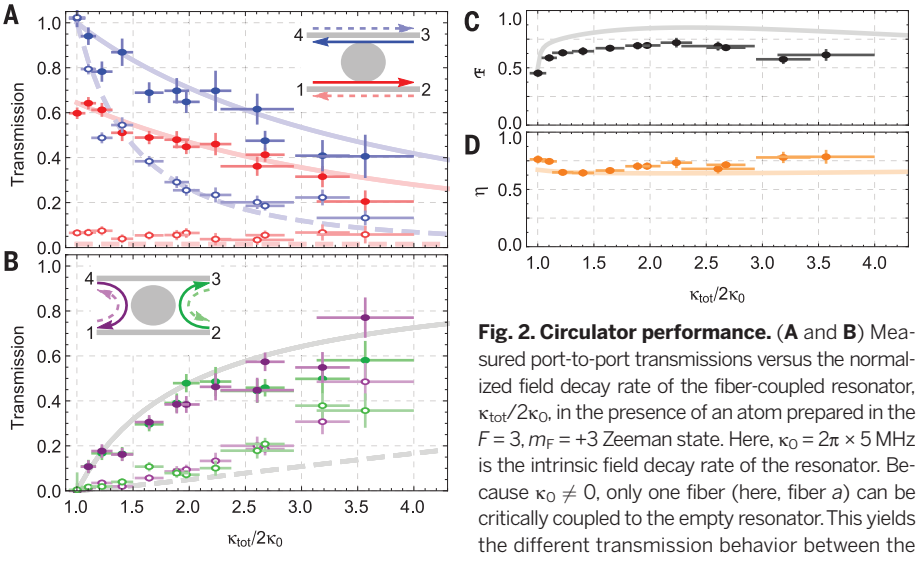

Fig. 2. Circulator performance. (**A** and **B**) Measured port-to-port transmissions versus the normalized field decay rate of the fiber-coupled resonator, $\kappa_{tot}/2\kappa_0$, in the presence of an atom prepared in the $F = 3$, $m_F = +3$ Zeeman state. Here, $\kappa_0 = 2\pi \times 5$ MHz is the intrinsic field decay rate of the resonator. Because $\kappa_0 \neq 0$, only one fiber (here, fiber *a*) can be critically coupled to the empty resonator. This yields the different transmission behavior between the cases $1 \leftrightarrow 2$ and $3 \leftrightarrow 4$. The solid circles indicate transmissions to the forward direction, and the open circles indicate transmissions to the backward direction; the color code follows that of the insets. (**C** and **D**) Operation fidelity $\mathcal{F}$ and photon survival probability η of the circulator, calculated from the data in (A) and (B). The lines are the predictions of our theoretical model (*26*), with the atom-resonator coupling strength $g_{ccw} = 2\pi \times 12$ MHz. The vertical error bars indicate $\pm 1\sigma$ statistical errors, and the horizontal error bars represent an estimate of the variation of κ_{tot} due to drifts of the fiber-resonator distances during the corresponding measurement.

To quantify the performance of the circulator, we calculated the overlap of the renormalized transmission matrix $\tilde{T} = (T_{i,j}/\eta_i)$, with the one expected for the ideal circulator, T^{id} (Fig. 3A). Here, $\eta_i = \sum_k T_{i,k}$ is the survival probability of a photon entering port i. Thus, the average operation fidelity of our circulator is

$$\mathcal{F} = \frac{\mathrm{Tr}[\tilde{T} \cdot T^{id^T}]}{\mathrm{Tr}[T^{id} \cdot T^{id^T}]} = 1 - \frac{1}{8}\sum_{i,j} \left| \tilde{T}_{i,j} - T^{id}_{i,j} \right| \quad (2)$$

This quantity—also called inquisition (*27*)—gives the probability of a correct circulator operation averaged over its eigenstates. The minimum fidelity is $\mathcal{F} = 0$, whereas $\mathcal{F} = 1$ is reached for ideal operation. For any reciprocal device ($\tilde{T} = \tilde{T}^T$), the fidelity is bound by $\mathcal{F} \leq 0.5$. In Fig. 2, C and D, we plot $\mathcal{F}$ and the average photon survival probability $\eta = \sum_i \eta_i/4$ as a function of κ_{tot}. The results show an optimum circulator performance for $\kappa_{tot}/2\kappa_0 = 2.2$, where $\mathcal{F} = 0.72 \pm 0.03$ and, at the same time, $\eta = 0.73 \pm 0.04$. The measured transmission matrix ($T_{i,j}$) for the optimum working point (Fig. 3B) shows good qualitative agreement with T^{id}. In order to demonstrate that the chiral atom-light coupling is at the origin of the nonreciprocal behavior, we also measured the transmission matrix without coupled atom and obtained a symmetric matrix (Fig. 3D). The circulator performance can also be quantified by the isolations, $I_i = 10\log(T_{i,i+1}/T_{i+1,i})$, of the four optical diodes formed between adjacent ports. For the optimum working point, we obtained $(I_i) = (10.9 \pm 2.5, 6.8 \pm 1.3, 4.7 \pm 0.7, 5.4 \pm 1.1)$ dB and an average insertion loss of $-10 \log \eta = 1.4$ dB.

In order to reverse the operation direction of the circulator, we then prepared the atom in the opposite Zeeman ground state, $F = 3$, $m_F = -3$ (*26*). This results in a complementary V-type level scheme (Fig. 1C, dashed arrows). For this case, we obtained the transmission matrix shown in Fig. 3C, again measured for the optimum fiber-resonator coupling rate. Here, we observed a fidelity with respect to the reversed circulator of $\mathcal{F} = 0.70 \pm 0.02$, an average photon survival probability of $\eta = 0.69 \pm 0.02$ corresponding to 1.6 dB average insertion loss, and optical isolations of $(I_i) = -(8.3 \pm 0.8, 4.9 \pm 0.7, 3.7 \pm 0.4, 5.6 \pm 0.5)$ dB. Taking into account the sign change, these results agree well with the values obtained for the atom in the $F = 3$, $m_F = +3$ state. State-of-the-art passive integrated optical circulators exhibit comparable isolations of ~12 dB, but they are subject to orders-of-magnitude-higher insertion losses of ~30 dB (*8*, *9*).

Last, in the regime of strong coupling, a single photon already saturates the atom (*14*, *17*, *28*). Thus, the transmission properties for the case of two photons simultaneously impinging on the circulator should strongly differ from the single-photon case. In order to demonstrate this quantum nonlinearity, we measured second-order

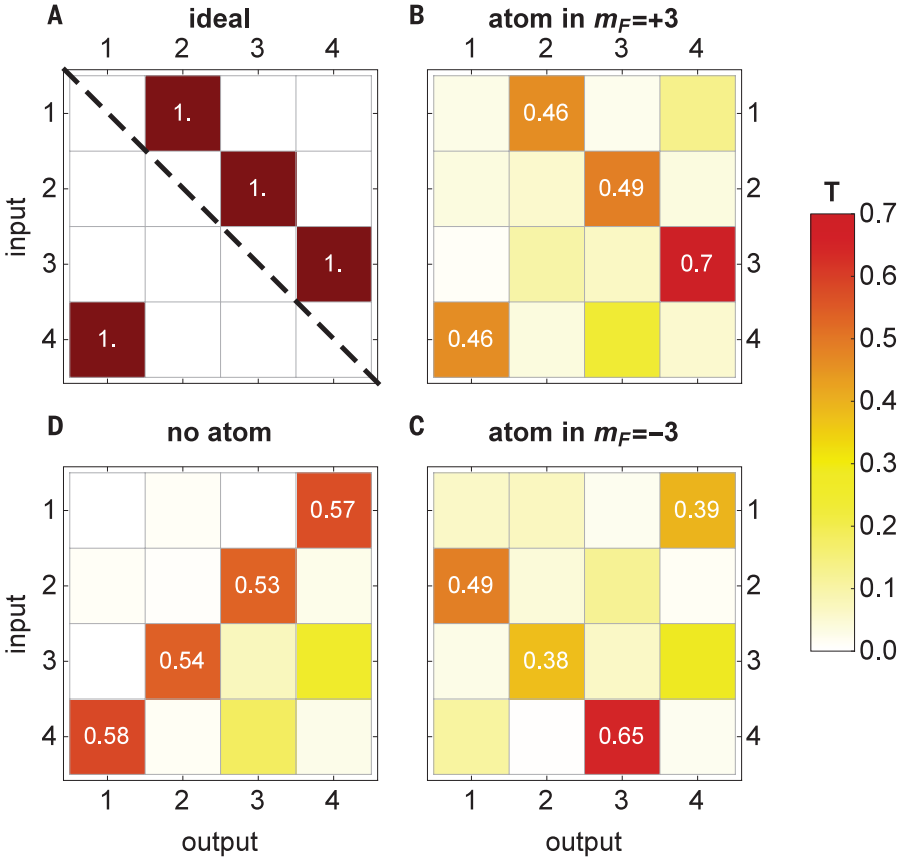

Fig. 3. Transmission matrices ($T_{i,j}$). The rows correspond to the input ports i and the columns to the output ports j. (**A**) Transmission matrix for an ideal cirulator. The broken symmetry with respect to the dashed line indicates the nonreciprocal character of the device. Transmission matrix measured for the atom prepared in (**B**) $F = 3$, $m_F = +3$ and (**C**) $F = 3$, $m_F = -3$ (reversed operation direction). For comparison, (**D**) shows the symmetric transmission matrix of the system measured without atom. For (B), (C), and (D), the fiber-resonator coupling was set to the optimal working point $\kappa_{tot}/2\kappa_0 = 2.2$. In (A) to (D), the four highest transmission values are given. All other values are below 0.28 (table S1).

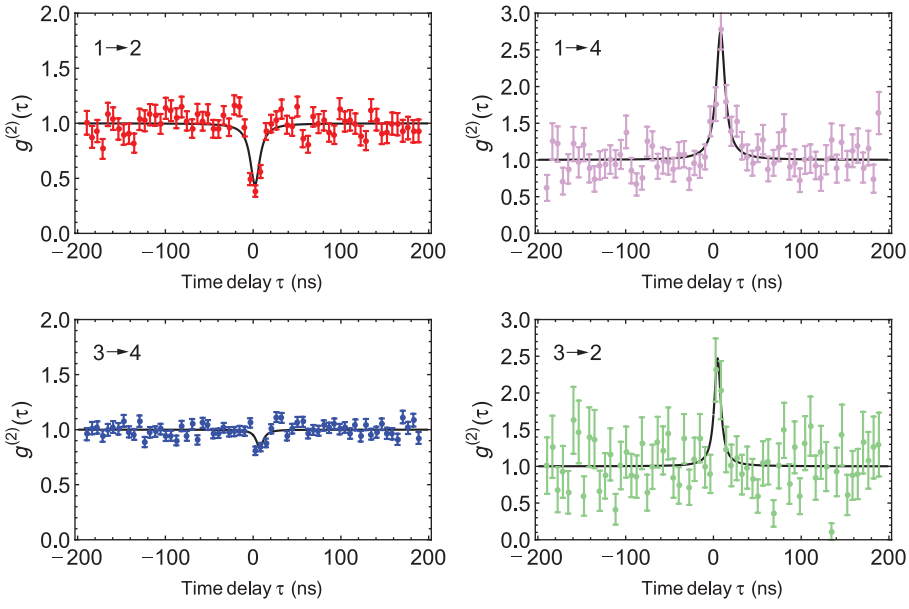

Fig. 4. Quantum nonlinearity of the circulator. Second-order correlation, $g^{(2)}(\tau)$, as a function of the detection time delay τ between pairs of photons, normalized so that $g^{(2)}(\tau) = 1$ for $\tau \gg 1/\kappa_{tot}$. The labels $i \rightarrow j$ indicate the input and output ports for the respective measurements. We use the same color code as in Fig. 2; the solid lines are guides to the eye. The error bars indicate the ±1σ statistical error.

correlation functions for all input-output combinations when the atom is prepared in $F = 3$, $m_F = +3$ (fig. S2). Those second-order correlations that yield the strongest signals are shown in Fig. 4. As expected (*26*), the strongest signals occur for the cases in which the photons couple into the ccw resonator mode. We observed photon antibunching for photons that remain in the initial fiber (forward direction of the circulator, $1 \rightarrow 2$, $3 \rightarrow 4$) and bunching for photons that are transmitted to the other fiber (backward direction of the circulator, $1 \rightarrow 4$, $3 \rightarrow 2$). This behavior illustrates the photon number–dependent routing capability; while individually arriving photons remain in their original fiber, simultaneously arriving photons are preferentially transferred to the other fiber.

The demonstrated circulator concept is useful for the processing and routing of classical signals at ultralow light levels in integrated optical circuits and networks. Beyond that, and in contrast to

dissipative nonreciprocal devices, a circulator that is controlled by a single quantum system also enables operation in coherent superposition states of routing light in one and the other direction, providing a route toward its application in future photonic quantum protocols. The demonstrated operation principle is universal in the sense that it can straightforwardly be implemented with a large variety of different quantum emitters provided that they exhibit circularly polarized optical transitions and that they can be spin-polarized. Using state-of-the-art WGM microresonators (*29*), one could realize a circulator with optical losses below 7% and close-to-unit operation fidelity (*26*). This would then allow one to almost deterministically process and control photons in an integrated optical environment. Arranging N circulators so that they form a linear array allows one to realize a $(2N + 2)$-port optical circulator. Moreover, two- and three-dimensional networks of quantum circulators are potential candidates for implementing lattice-based quantum computation (*30*). Such networks would enable the implementation of artificial gauge fields for photons (*31*–*33*), in which a nonlinearity at the level of single quanta allows for the flux to become a dynamical degree of freedom that interacts with the particles themselves (*34*).

REFERENCES AND NOTES

1. B. J. H. Stadler, T. Mizumoto, *IEEE Photonics J.* **6**, 1–15 (2014).
2. K. Gallo, G. Assanto, K. R. Parameswaran, M. M. Fejer, *Appl. Phys. Lett.* **79**, 314 (2001).
3. L. Fan *et al.*, *Science* **335**, 447–450 (2012).
4. B. Peng *et al.*, *Nat. Phys.* **10**, 394–398 (2014).
5. H. Lira, Z. Yu, S. Fan, M. Lipson, *Phys. Rev. Lett.* **109**, 033901 (2012).
6. L. D. Tzuang, K. Fang, P. Nussenzveig, S. Fan, M. Lipson, *Nat. Photonics* **8**, 701–705 (2014).
7. J. Kim, M. C. Kuzyk, K. Han, H. Wang, G. Bahl, *Nat. Phys.* **11**, 275–280 (2015).
8. Y. Shoji, T. Mizumoto, *Sci. Technol. Adv. Mater.* **15**, 014602 (2014).
9. D. Huang *et al.*, *Conference on Lasers and Electro-Optics* (2016), p. SM3E.1.
10. N. Gisin, R. Thew, *Nat. Photonics* **1**, 165–171 (2007).
11. M. A. Nielsen, I. L. Chuang, *Quantum Computation and Quantum Information* (Cambridge Univ. Press, 2011).
12. R. P. Feynman, *Int. J. Theor. Phys.* **21**, 467–488 (1982).
13. M. Pöllinger, A. Rauschenbeutel, *Opt. Express* **18**, 17764–17775 (2010).
14. D. O'Shea, C. Junge, J. Volz, A. Rauschenbeutel, *Phys. Rev. Lett.* **111**, 193601 (2013).
15. C. Junge, D. O'Shea, J. Volz, A. Rauschenbeutel, *Phys. Rev. Lett.* **110**, 213604 (2013).
16. P. Lodahl *et al.*, https://arxiv.org/abs/1608.00446 (2016).
17. I. Shomroni *et al.*, *Science* **345**, 903–906 (2014).
18. S. Rosenblum *et al.*, *Nat. Photonics* **10**, 19–22 (2016).
19. C. Sayrin *et al.*, *Phys. Rev. X* **5**, 041036 (2015).
20. H. J. Metcalf, P. van der Straten, *Laser Cooling and Trapping* (Springer, 1999).
21. D. Jalas *et al.*, *Nat. Photonics* **7**, 579–582 (2013).
22. K. Xia *et al.*, *Phys. Rev. A* **90**, 043802 (2014).
23. E. J. Lenferink, G. Wei, N. P. Stern, *Opt. Express* **22**, 16099–16111 (2014).
24. I. Söllner *et al.*, *Nat. Nanotechnol.* **10**, 775–778 (2015).
25. C. Gonzalez-Ballestero, E. Moreno, F. J. Garcia-Vidal, A. Gonzalez-Tudela, https://arxiv.org/abs/1608.04928 (2016).
26. Materials and methods are available as supplementary materials on *Science* Online.
27. A. G. White *et al.*, *J. Opt. Soc. Am. B* **24**, 172 (2007).
28. J. Volz, M. Scheucher, C. Junge, A. Rauschenbeutel, *Nat. Photonics* **8**, 965–970 (2014).
29. M. Pöllinger, D. O'Shea, F. Warken, A. Rauschenbeutel, *Phys. Rev. Lett.* **103**, 053901 (2009).
30. R. Raussendorf, H. J. Briegel, *Phys. Rev. Lett.* **86**, 5188–5191 (2001).
31. J. Koch, A. A. Houck, K. L. Hur, S. M. Girvin, *Phys. Rev. A* **82**, 043811 (2010).
32. M. Hafezi, P. Rabl, *Opt. Express* **20**, 7672–7684 (2012).
33. M. Schmidt, S. Kessler, V. Peano, O. Painter, F. Marquardt, *Optica* **2**, 635 (2015).
34. S. Walter, F. Marquardt, *New J. Phys.* **18**, 113029 (2016).

ACKNOWLEDGMENTS

The authors are grateful to J. Simon and M. Levy for helpful discussions. We gratefully acknowledge financial support by the Austrian Science Fund (FWF; SFB FoQuS project no. F 4017 and DK CoQuS project no. W 1210-N16) and the European Commission (IP SIQS, no. 600645). A.H. acknowledges financial support from the Austrian Science Fund (FWF; Meitner Program Project M 1970).

SUPPLEMENTARY MATERIALS

www.sciencemag.org/content/354/6319/1577/suppl/DC1
Materials and Methods
Figs. S1 and S2
Table S1
Reference (*35*)

13 September 2016; accepted 21 November 2016
Published online 8 December 2016
10.1126/science.aaj2118

NANOMATERIALS

Emergence of hierarchical structural complexities in nanoparticles and their assembly

Chenjie Zeng,[1] Yuxiang Chen,[1] Kristin Kirschbaum,[2] Kelly J. Lambright,[2] Rongchao Jin[1]*

We demonstrate that nanoparticle self-assembly can reach the same level of hierarchy, complexity, and accuracy as biomolecules. The precise assembly structures of gold nanoparticles (246 gold core atoms with 80 *p*-methylbenzenethiolate surface ligands) at the atomic, molecular, and nanoscale levels were determined from x-ray diffraction studies. We identified the driving forces and rules that guide the multiscale assembly behavior. The protecting ligands self-organize into rotational and parallel patterns on the nanoparticle surface via C-H···π interaction, and the symmetry and density of surface patterns dictate directional packing of nanoparticles into crystals with orientational, rotational, and translational orders. Through hierarchical interactions and symmetry matching, the simple building blocks evolve into complex structures, representing an emergent phenomenon in the nanoparticle system.

Hierarchical self-assembly of nanoparticles (NPs) into complex architectures across different length scales is an important capability in nanotechnology (*1*–*4*), especially for the bottom-up fabrication for electronics, sensors, energy conversion, and storage devices. Such self-assembly can be driven by entropy-dictated maximization of the packing density, as demonstrated in close packing of spheres, binary NPs, rods, and hard polyhedrons (*5*–*9*). Interparticle interactions, such as the electrostatic attraction (*10*), cDNA binding (*11*, *12*), and patchy NP surfaces (*13*–*15*), have also been exploited to guide assembly into diverse lattice structures. Despite these advances, NP assembly has not achieved the same level of atomic accuracy as in biological systems.

We now demonstrate that NP-assembled structures can reach the same hierarchy and atomic accuracy as biomolecules at the interparticle and intraparticle levels. Through crystallization of uniform 2.2-nm gold NPs bearing *p*-methylbenzenethiolate (*p*-MBT) surface ligands [Au_{246}(*p*-MBT)$_{80}$], we fully resolve the entire self-assembled structures at atomic (packing of gold atoms), molecular (packing of surface ligands), and nanoscale (packing of NPs) levels by single-crystal x-ray diffraction (SC-XRD) (*16*). The precise structural information across scales allows an in-depth examination of the forces and the rules that govern the assembly behavior at each level. We reveal that the simple structure of protecting ligands can generate complex patterns on the NP surfaces, and the symmetry and density of the surface patterns further guide the packing of NPs into lattices with orientational, rotational, and translational order.

The Au_{246}(*p*-MBT)$_{80}$ NPs were synthesized by a two-step "size-focusing" method (*16*). Briefly, the ligand-coated NPs in a narrow size range from ~10 to ~70 kilodaltons were first made, and then the size focusing process gradually led to the stable Au_{246}(*p*-MBT)$_{80}$ NPs (figs. S1 and S2). The as-obtained product (~90% purity) was subject to further solvent fractionation to reach molecularly pure Au_{246} NPs. Optical absorbance spectra showed a prominent peak at 470 nm and several weak humps at 400 and 600 nm (fig. S3), indicating the nonplasmonic nature of the Au_{246}(*p*-MBT)$_{80}$ NPs. Single crystals were grown by diffusion of antisolvent (acetonitrile) into a toluene solution of the pure Au_{246} NPs. The structure was determined at the resolution of 0.96 Å by SC-XRD

[1]Department of Chemistry, Carnegie Mellon University, Pittsburgh, PA 15213, USA. [2]Department of Chemistry and Biochemistry, University of Toledo, Toledo, OH 43606, USA.
*Corresponding author. Email: rongchao@andrew.cmu.edu

Quantum optical circulator controlled by a single chirally coupled atom

Michael Scheucher, Adèle Hilico, Elisa Will, Jürgen Volz and Arno Rauschenbeutel (December 8, 2016)

Science **354** (6319), 1577-1580. [doi: 10.1126/science.aaj2118]
originally published online December 8, 2016

Editor's Summary

A quantum optical circulator

A circulator is a passive three- or four-port device that routes signals according to a simple protocol: If the ports are numbered in ascending order, a signal that enters the circulator through port 1, 2, 3, or 4 exits it through port 2, 3, 4, or 1, respectively. Scheucher *et al.* demonstrate an integrated optical circulator that operates by using the internal quantum state of a single atom (see the Perspective by Munro and Nemoto). Moreover, the routing can be reversed by flipping the atomic spin. Such an integrated optical device may be important for routing and processing quantum information in scalable integrated optical circuits.

Science, this issue p. 1577; see also p. 1532

Science (print ISSN 0036-8075; online ISSN 1095-9203) is published weekly, except the last week in December, by the American Association for the Advancement of Science, 1200 New York Avenue NW, Washington, DC 20005.